Macromolecules **2008**, *41*, 5729−5743

Photo-Oxidation of High Performance Epoxy Networks: Correlation between the Molecular Mechanisms of Degradation and the Viscoelastic and Mechanical Response

Pellegrino Musto,* Giuseppe Ragosta, Mario Abbate, and Gennaro Scarinzi

Institute of Chemistry and Technology of Polymers, National Research Council of Italy, via Campi Flegrei, 34, 80078 Pozzuoli (NA), Italy

Received March 10, 2008; Revised Manuscript Received May 12, 2008

ABSTRACT: The photo-oxidative degradation of a highly cross-linked epoxide/diamine network has been investigated by FTIR spectroscopy, dynamic-mechanical thermal analysis (DMTA) and compressive mechanical tests. The FTIR measurements allowed us to monitor the degradation process and to obtain reliable kinetic data. Two dimensional infrared (2D IR) correlation spectroscopy, was employed to analyze the spectra collected as a function of time. This approach effectively enhanced the spectral resolution and revealed details about the reaction mechanism hardly detectable in the one-dimensional, frequency domain. In particular, the sites of initiation of the auto-oxidative sequence were identified, and the main pathways through which the degradation reaction proceeds were proposed. Dynamic-mechanical measurements performed in a multifrequency mode were used to reveal the effect of the photo-oxidative degradation on the relaxation processes of the epoxy network. It was found that the T_g decreases with increasing the exposure time. An analogous trend was found for the storage modulus, E', at temperatures above the glass transition. The overall cross-linking density was found to decrease as a consequence of the chain scission reactions. A marked reduction of the mechanical performances of the material was evidenced at high exposure times, especially in terms of yield-strength and strain.

Introduction

Due to their outstanding properties, epoxy resins are a class of materials of primary technological interest. In particular, these resins are characterized by high resistance to chemicals and corrosive agents, good mechanical properties, excellent adhesion to various substrates, low shrinkage upon cure and ease of processing under a wide range of conditions.[1–4]

In recent years, the ever increasing need for materials for specialized applications has driven significant research efforts toward the development of high-performance epoxies to be employed, for example, as adhesives, specialized coatings for aggressive environments (nuclear waste management) and substrates or encapsulants for circuit boards in the electronic industry.[3–6] However, the most important application of epoxy resins is still in the transportation industry, particularly in such areas as civil and military aircraft industry, aerospace and in the marine and automotive sectors.[2,4] Clearly, one of the main concerns when dealing with these applications is the sensitivity to natural weathering, i.e., the effect of prolonged exposure to direct sunlight in an atmospheric environment. It has been demonstrated[8,9] that, under these conditions, bifunctional epoxies based on diglycidyl ether of bisphenol A (DGEBA) undergo quite extensive photodegradation which brings about a considerable deterioration of mechanical performances and, ultimately, the failure of the item. The photo-oxidation of DGEBA resins has been investigated by numerous authors.[7–15] In particular, it has been shown that the sensitivity of these materials to UV radiation is dependent on their molecular structure, i.e., on the hardener used, and that the initiating species derives from the phenoxy part, while the propagation depends mainly on the amine concentration and on the electron density at the nitrogen atom.[11–15]

Much less information is available on the photoaging behavior of resins based on tetraglycidyl-4,4′ diaminodiphenylmethane (TGDDM), although this monomer, cured with the aromatic diamine hardener 4,4′-diaminodiphenyl sulfone (DDS) represents the preferred matrix for carbon fiber composites in aerospace applications.[4] This epoxy formulation is generally used as structural material, whereas DGEBA based resins, because of their lower rigidity are preferred as coatings. Most of the literature on TGDDM/DDS systems focus on thermal-oxidative degradation, which takes place at temperatures above 200 °C and may occur through different reaction mechanisms with respect to photo-oxidation, especially in terms of initiation, albeit both are radical processes involving similar reagents and, as such, may share some relevant features.

Recent experiments[16,17] carried out with the use of *time-resolved* FTIR spectroscopy showed that, under thermo-oxidative conditions, the weakest part of the network is the aliphatic segment. Despite a lower sensitivity to degradation, aromatic groups are also attacked, although their relative stability depends on the local chemical environment. Oxygen attack causes the formation of several oxygenated species, among which aldehydes, ketones and amide groups were spectroscopically identified.

The present contribution is aimed at investigating the kinetics and mechanism of the photodegradation process of a TGDDM/DDS network in an experimental setup simulating the actual service conditions. The motivation for this work lies in the lack of information regarding this specific system, its technological relevance, and in the fact that its molecular structure is considerably different from that of the DGEBA resins, whose photoaging behavior has been investigated in much more detail. A deeper understanding of the photo-oxidative processes governing the degradation of this material under service conditions, represents a prerequisite for the development of a suitable stabilization strategy.

The mechanisms proposed on the basis of the experimental results are discussed in comparison to those of the thermo-oxidative degradation to highlight differences and similarities. Moreover, the effect of the photodegradation on the viscoelastic response of the material and on its mechanical performances is studied in the light of the changes taking place within the

---

* Corresponding author. E-mail: musto@ictp.cnr.it.

10.1021/ma8005334 CCC: $40.75

molecular structure of the network. The experimental approaches used throughout are Fourier Transform infrared spectroscopy for the kinetic and mechanistic analysis, and dynamic-mechanical spectroscopy and compressive mechanical tests for the viscoelastic behavior and the mechanical properties, respectively.

Experimental Section

1. Materials. The epoxy resin was a commercial grade tetraglycidyl-4,4′-diaminodiphenylmethane (TGDDM) supplied by Ciba Geigy (Basel, Switzerland). This reagent has an epoxy equivalent weight of 124.1 g equiv^{-1}, measured by potentiometric titration. It is found that the actual number of epoxy groups is 15% by mol lower than the stoichiometric number based on the molecular structure *a*, and this can be attributed to oligomerization, which is confirmed by the presence of a readily detectable hydroxyl band in the 3600−3300 cm^{-1} range of the FTIR spectrum of the uncured resin. The curing agent was 4,4′-diaminodiphenylsulfone (DDS) from Aldrich (Milwaukee, WI), having a reported degree of purity higher than 95%. The reagents were used as received, without further purification. The chemical formulas of the resin components are reported below:

a) TGDDM: tetraglycidyl-4,4'-diaminodiphenylmethane

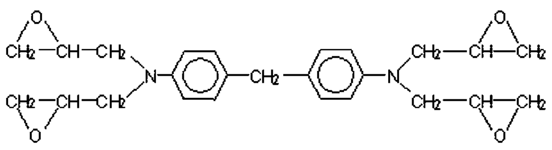

b) DDS: 4,4'-diaminodiphenylsulfone

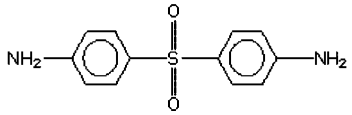

Thirty grams of DDS was dissolved in 100 g of TGDDM at 120 °C, degassed under vacuum, and poured between two stainless steel plates. The first step of the curing schedule was conducted at 140 °C for 16 h, followed by a postcuring step at 200 °C for 4 h. The density of the fully cured network was 1.259 g/cm^3, as determined by a density gradient column.

In order to obtain infrared spectra suitable for quantitative analysis, the intensity of the peaks of interest must not exceed absorbance values in the range 1.5−1.8 units. Films for these measurements (5 to 10 μm of thickness) were prepared by dissolving TGDDM and DDS in the appropriate amounts, in CH_2Cl_2 (total concentration 5.0 wt %), followed by casting on a KBr disk. After solvent removal (12 h in a vacuum oven at 35 °C) the free surface of the cast film was covered with a second KBr disk of the same size. Curing (140 °C, 16 h) and postcuring (200 °C, 4 h) were carried out under N_2 atmosphere to prevent oxidation. Finally, the two KBr disks were dissolved in distilled water and a free-standing film was obtained.

2. Techniques. Photoaging experiments were carried out in an environmental chamber (weatherometer Angelantoni Mod. Challenge 250E) equipped with a UV bulb lamp mainly emitting in the spectral range of 320−600 nm (simulating the solar spectrum). The device was equipped with temperature and relative humidity controls which were set to 50 °C and 50%, respectively. Transmission FTIR spectra were obtained using a Perkin-Elmer System 2000 spectrometer. This instrument was fitted with a germanium/KBr beam splitter and a deuterated tryglycine sulfate (DTGS) wide-band detector. The instrumental parameters adopted for the spectral collection were as follows: resolution 4 cm^{-1}, scan speed [i.e., Optical Path Difference (OPD) velocity] = 0.20 cm s^{-1}, and spectral range 4000−350 cm^{-1}. For each spectrum, 32 consecutive scans were averaged in order to improve the signal-to-noise ratio.

Dynamic−mechanical tests were carried out on samples with dimensions 50 × 10 × 1.0 mm using a Perkin-Elmer Pyris Diamond DMA apparatus. The geometry of deformation was the single-cantilever bending mode, applying a strain of 1%. The tests were performed in the scanning temperature mode, in the range from −150 to +350 °C at a heating rate of 3 °C/min. At each temperature the frequency was scanned from 0.05 to 20 Hz. The storage modulus (E'), loss modulus (E''), and loss factor (tan δ) were recorded.

Mechanical tests were performed using a universal testing machine (Instron model 4505). The yield strength was measured in compression on specimens 12 × 6.0 × 4.0 mm, loaded along the length. The tests were carried out at ambient temperature and at a cross-head speed of 1 mm/min. Due to the absence of a definite maximum in the load/deformation curves the yield strength was estimated as the stress corresponding to the 5% offset strain from the elastic strain.

3. Data Analysis. In the case of unresolved, multicomponent bands the individual peaks were separated by a curve resolving algorithm based on the Levenberg−Marquardt method.[18] In order to reduce the number of adjustable parameters and to ensure the uniqueness of the result, the baseline, the band shape and the number of components were fixed. The number of components was evaluated by both a visual inspection of abrupt changes in the slope of the experimental line-shape and by second-derivative analysis. The program was then allowed to calculate, by a nonlinear curve fitting of the data, the height, the full width at half-height (fwhh) and the position of the individual components. The peak function used throughout was a mixed Gaussian−Lorentzian line shape.[19]

Before performing cross-correlation analysis, the experimental spectra were preprocessed to avoid the occurrence of artifacts due to baseline instabilities and other nonselective effects. The frequency region of interest (1800−1440 cm^{-1}) was truncated and was subjected to a linear baseline correction, followed by offset to the zero absorbance value. Generalized 2D IR analysis was performed by a computer program written in house within the Grams/32 environment (Galactic Industries Co., Salem, NH), using the associated programming language Array Basic. Since the spectra were collected at unevenly spaced increments of time, the synchronous [$\Phi(\nu_1,\nu_2)$] and asynchronous [$\Psi(\nu_1,\nu_2)$] spectra were calculated according to the algorithm reported in ref 20 for this specific case:

$$\Phi(\nu_1, \nu_2) = \frac{1}{2(t_m - t_1)} \sum_{j=1}^{m} \tilde{y}_j(\nu_1)\tilde{y}_j(\nu_2)(t_{j+1} - t_{j-1})$$

$$\Psi(\nu_1, \nu_2) = \frac{1}{2(t_m - t_1)} \sum_{j=1}^{m} \tilde{y}_j(\nu_1)\tilde{z}_j(\nu_2)(t_{j+1} - t_{j-1}) \quad \text{(A1)}$$

where $\tilde{y}_j(\nu)$is the dynamic spectrum collected at time t_j[17,20] and $\tilde{z}_j(\nu_2)$is the discrete Hilbert transform of unevenly spaced data sets, which can be expressed, in compact form as[20]

$$\tilde{z}_j(\nu_2) = \sum_{k=1}^{m} N_{jk}\tilde{y}_k(\nu_2) \quad \text{(A2)}$$

In the above expression N_{jk} is the element of the Hilbert−Noda transformation matrix for unevenly spaced data sets, i.e.

$$N_{jk} = \begin{cases} 0 & \text{for } j = k \\ \dfrac{t_{k+1} - t_{k-1}}{2\pi(t_k - t_j)} & \text{otherwise} \end{cases} \quad \text{(A3)}$$

The notation adopted to identify the correlation peaks appearing in the 2D spectra was that described in ref 17.

Results and Discussion

1. FTIR Spectroscopy. *1.1. Spectral Interpretation and Kinetic Analysis.* In Figure 1, trace A is reported the FTIR spectrum of a fully cured TGDDM/DDS resin in the 4000−350 cm^{-1} wavenumber range. The spectrum has been thoroughly discussed in several literature studies[16,17,21,22] and, in particular, in refs 16 and 21 assignments have been proposed for most

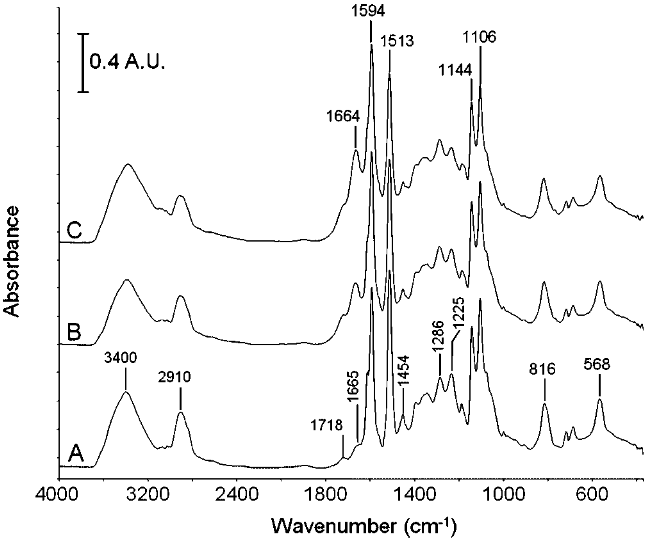

Figure 1. Transmission FTIR spectra in the wavenumber range 4000−350 cm^{-1} of the TGDDM/DDS resin before and after photo-degradation. Trace A: initial spectrum. Trace B: spectrum after 1.5 10^4 min. Trace C: spectrum after 3.1 × 10^4 min. The spectra have been arbitrarily shifted along the *Y* axis to facilitate comparison.

peaks. In the present context, we will review those assignments most relevant to the molecular level description of the photo-oxidative process.

An intense and characteristically broadband centered at 3400 cm^{-1} originates from the H-bonded hydroxyl groups of the network, plus a contribution due to absorbed water. The υ(CH) modes give rise to a complex band at around 2910 cm^{-1} whose components are fully overlapped to each other. It is anticipated that, due to the absence of resolution, no detailed structural information is available from the analysis of this band other than a gradual decrease of its intensity (i.e., a reduction of the overall C−H concentration) with exposure time.

Two low intensity absorptions are detected at 1718 and 1665 cm^{-1}, attributed, respectively, to ketonic/aldehydic carbonyls and amide carbonyls formed in trace amounts during the high temperature curing stage.[21] This thermo-oxidative reaction takes place albeit the curing process is carried out under N_2 atmosphere (see experimental), possibly due to residual oxygen trapped in the uncured monomers admixture. A partially resolved doublet at 1613−1594 cm^{-1} is associated, respectively, to the aromatic ring stretching of the TGDDM and the DDS units (see Scheme 1). A further aromatic peak at 1513 cm^{-1} arise from the ring semicircle stretching of the TGDDM unit. The pattern of intense aromatic absorptions in the 1640−1480 cm^{-1} interval is particularly useful in that it provides information on the relative stability of the two substituted benzene rings in the different chemical environments. More on this later. A peak at 1454 cm^{-1} has been associated with the in-plane bending of CH_2 groups while the out-of-phase and in-phase stretching modes of the SO_2 group give rise to peaks at 1286 and 1144 cm^{-1}, respectively. Finally, a multicomponent absorption at 816 cm^{-1} has been assigned to the δ(Ar−H) modes of the various aromatics, while a medium intensity band at 568 cm^{-1} has been attributed to the in-plane bending vibration of the SO_2 group.

The substantial changes occurring in the FTIR spectrum with exposure time are demonstrated in Figure 1, traces B and C, and in Figure 2, parts A−C, which refer, respectively, to the υ(CH) range (3120−2670 cm^{-1}), the carbonyl−aromatic range (1900−1420 cm^{-1}) and the 940−480 cm^{-1} interval. It is apparent that the concentration of aliphatic groups decreases steadily (reduction of the absorbance area of the bands at 2900 and 1454 cm^{-1}). The concentration of the substituted benzene rings also declines, but a significant difference is observed between the reduction of the 1513 cm^{-1} band (TGDDM aromatics) and that of the band at 1594 cm^{-1} (DDS aromatics). The resolution of the doublet at 1613−1594 cm^{-1} worsen, owing to a gradual widening of both components upon degradation. The two carbonyl bands centered at 1718 and 1665 cm^{-1} increase substantially, with the latter becoming progressively predominant. The spectral data displayed in Figure 2, parts A−C, allow a quantitative description of the photo-oxidation process in terms of relative conversion and reaction rates for the reactive groups that are consumed, or as rate of formation for the functionalities (carbonyls) produced upon the oxygen attack on the polymer network. Thus, assuming a negligible change of the film thickness, the relative conversion at time *t*, α_t, can be expressed spectroscopically as:

$$\alpha_t = \frac{C_0 - C_t}{C_0} = 1 - \frac{C_t}{C_0} = 1 - \frac{A_t}{A_0} \tag{1}$$

The reaction rates can be estimated once an appropriate kinetic model has been identified, as in the forthcoming discussion. In order to get a reliable evaluation of the peaks' absorbance, it is necessary to achieve the full resolution of the different components and to identify a reproducible baseline. Several approaches have been employed in the present contribution, depending on the characteristics of the spectral profiles under investigation. Thus, spectral subtraction in the 1900−1350 cm^{-1}, followed by the quantitative analysis described in detail in ref 16, allowed us to fully resolve the doublet at 1613−1594 cm^{-1}, as demonstrated in Figure 3, where the baseline to evaluate the peak heights is also shown. The two carbonyl components were resolved by use of least-squares curve fitting (LSCF) analysis, as shown in Figure 4, while, for the peaks at 1513 and 1454 cm^{-1}, the peak height was directly evaluated from the as-collected spectra.

The relative conversion vs time curves for the peaks at 1454 cm^{-1} (CH_2 groups) 1593 cm^{-1} (DDS aromatics), and 1513 cm^{-1} (TGDDM aromatics) are reported, respectively, in Figure 5 and in Figure 6, curves A and B. In Figure 7 are shown the absorbance vs time profiles for the carbonyl components at 1725 and 1665 cm^{-1}. A phenomenological model widely adopted to describe heterogeneous processes governed by phase-boundary reaction mechanisms has the form:

$$\frac{d\alpha}{dt} = Ae^{-E_a/RT}(1-\alpha)^n \tag{2}$$

Equation 2 is meaningful only for discrete values of *n*.[6,23,24] For $n = 1$, integration of eq 2 yields the expression:

$$\alpha_t = \alpha_f(1 - e^{-kt}) \tag{3}$$

where α_f is the final conversion, i.e the conversion at $t \rightarrow \infty$ and $k = Ae^{-E_a/RT}$ is the Arrhenius-type, kinetic constant.

Furthermore, recalling that $\alpha_t = A_0 - A_t/A_0$, the conversion equation can be written as:

$$A_0 - A_t = (A_0 - A_f)(1 - e^{-kt}) \tag{4}$$

or

$$A_t = A_f(1 - e^{-kt}) \tag{5}$$

for the reaction products when A_0 is zero, i.e., when no reaction products are present at $t = 0$.

The experimental α *vs time* (or *A vs time*) curves for the different reactive groups were tested according to eq 2 for integer values of *n* comprised between 1 and 4. It was found that for all profiles the best fit was achieved with a first order model ($n = 1$), which yielded a very satisfactory description of the experimental data. Only in the case of the curve relative to

Scheme 1

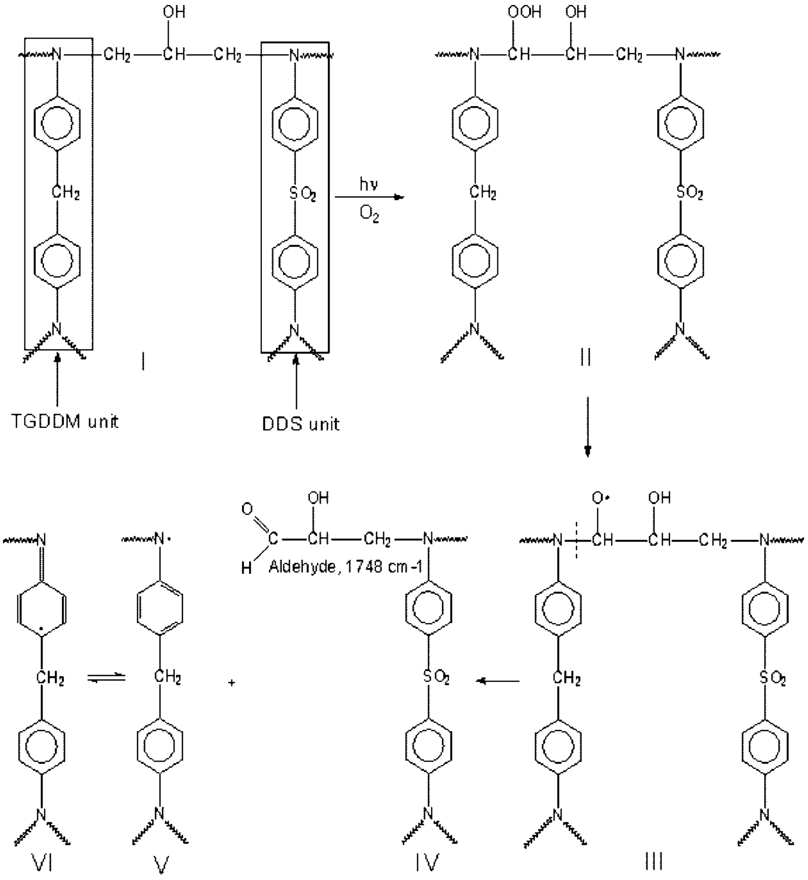

the amide group the discrepancy between the model simulation and the actual data was higher, but this is to be ascribed to the uncertainty introduced by the data-analysis method used in this case (i.e., LSCF). This conclusion is supported by the observation that the standard error is randomly distributed within the data set.

The curves obtained by eqs 3 (or 5 where appropriate) through a nonlinear least-squares regression of the experimental data are reported, as continuous lines, in Figures 5–7. The kinetic parameters (i.e., rate constants and final conversion) evaluated by the model are collectively reported in Table 1. It is apparent that the kinetic constant relative to the consumption of CH_2 groups has a value close to that relative to the formation of amide groups, while the aldehyde/ketone carbonyls and the two aromatic rings display significantly lower k values. In particular, the carbonyl groups and the TGDDM aromatics display close k values, while the kinetic constant for the DDS aromatics is about 1.7 times lower. The k values hold information on the relative reactivity of the different groups, and can be employed to rank their photo-oxidative stability. Thus, from the kinetic analysis, it emerges that the methylene groups are the more susceptible to photo-oxidation and, possibly, the site of initiation of the whole process. The reaction of the methylene is the rate controlling step of the pattern that yields the amide groups (comparable rate constants). The photo-oxidative mechanism producing the depletion of the TGDDM aromatic rings is likely alternative to that yielding amide groups and is directly related to the path giving rise to aldehyde/ketone carbonyls. The DDS aromatic rings are significantly more stable that the TGDDM aromatics.

1.2. Two-Dimensional Correlation Spectroscopy. Toward a more complete interpretation of the molecular information contained in the infrared spectra, it is necessary to improve the resolution and to get further details about the dynamic behavior of the investigated system. To this end, the 2D-FTIR spectroscopy, was demonstrated to be particularly powerful and versatile.[25–29] This method relies on the well established principles of time-series analysis: it consists in applying an external perturbation to a system initially at equilibrium, and in analyzing its response in terms of the variation of spectroscopic signals. The correlation analysis performed on the spectral response of the system allows one to evaluate the covariance of two variables (peak absorbances, in the present case) as they evolve as a function of a third common variable related to the perturbation function (time, in the present case). Two correlation spectra are produced by the 2D-FTIR analysis, i.e. one synchronous and one asynchronous spectrum. The former displays autopeaks (always positive) along the main diagonal (i.e., at coordinates ν_i,ν_i) and cross-peaks at off-diagonal positions. If, as in the present case, the dynamic component of the response function of the system is an exponential decay, the autopeaks' intensity reflects the susceptibility of the IR signals to the perturbation, while the cross-peaks appear at coordinates ν_i,ν_j, for any couple of IR peaks at ν_i and ν_j undergoing intensity changes during the sampling interval, irrespective of their rate of change. The cross-peaks are positive if the correlated signals change in the same sense (they both increase or decrease) and are negative otherwise.

In the asynchronous spectrum there are no autopeaks; a cross-peak at ν_i,ν_j corresponds to two IR signals changing at different rates, insofar as when two signals evolve with the same rate they produce zero correlation intensity. This provides further resolution enhancement and superior specificity for the asynchronous map. The sign of the correlation peaks is also relevant in that it provides information about the relative rate of change of the two IR signals involved, according to the so-called Noda's rules.[25,26] Thus, an asynchronous cross-peak located at coordinates ν_i,ν_j is positive if the intensity change at ν_i is accelerated

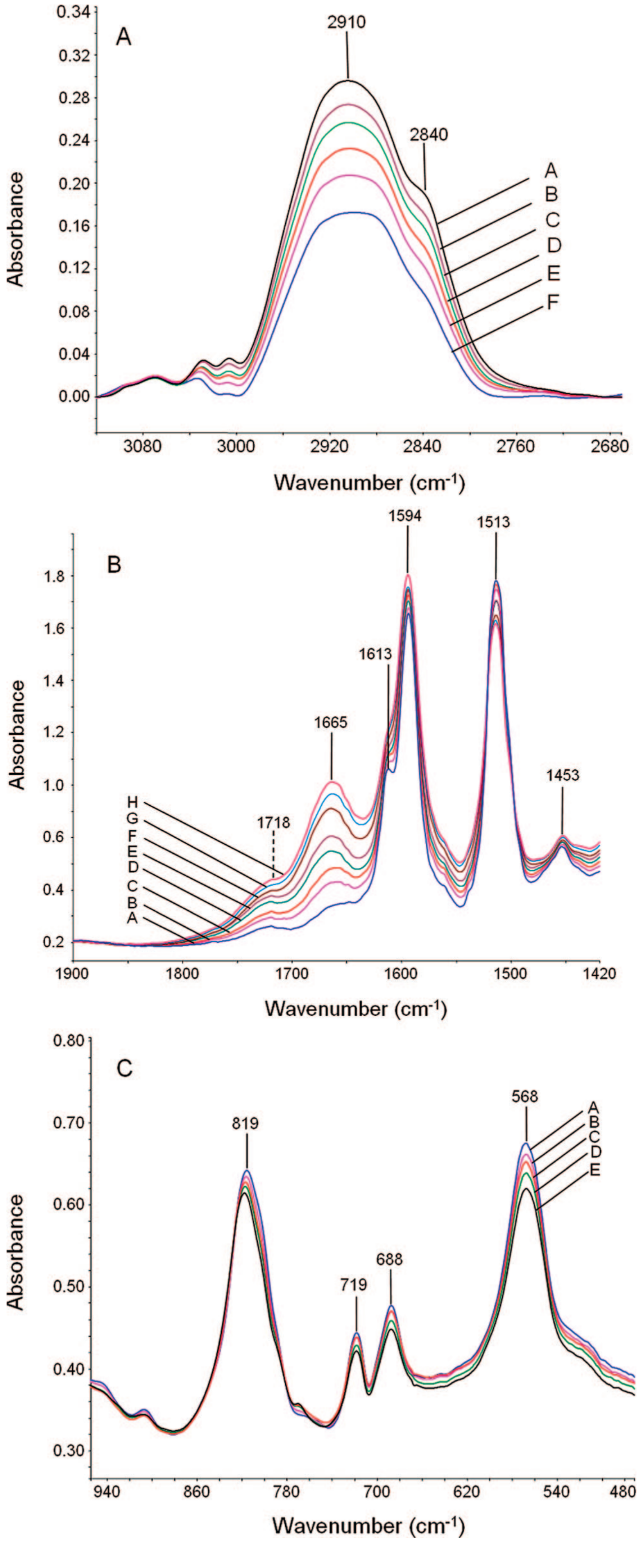

Figure 2. A. Transmission FTIR spectra in the wavenumber range 3120−2180 cm^{-1}, collected at various times during photodegradation. Key: trace A, collection time, $t = 0$ min; trace B, $t = 1.4 \times 10^3$ min; trace C, $t = 4.1 \times 10^3$ min; trace D, $t = 1.4 \times 10^4$ min; trace E, $t = 2.1 \times 10^4$ min; trace F, $t = 3.5 \times 10^4$ min. B. Transmission FTIR spectra in the wavenumber range 1900−1420 cm^{-1}, collected at various times during photodegradation. Key: trace A, collection time, $t = 0$ min; trace B, $t = 1.4 \times 10^3$ min; trace C, $t = 2.5 \times 10^3$ min; trace D, $t = 4.1\ 10^3$ min; trace E, $t = 1.4\ 10^4$ min; trace F, $t = 2.1 \times 10^4$ min; trace G, $t = 2.8 \times 10^4$ min; trace H, $t = 3.5 \times 10^4$ min. C. Transmission FTIR spectra in the wavenumber range 950−470 cm^{-1}, collected at various times during photodegradation. Key: trace A, collection time, $t = 0$ min; trace B, $t = 4.1 \times 10^3$ min; trace C, $t = 1.4 \times 10^4$ min; trace D, $t = 2.1 \times 10^4$ min; trace E, $t = 3.5 \times 10^4$ min.

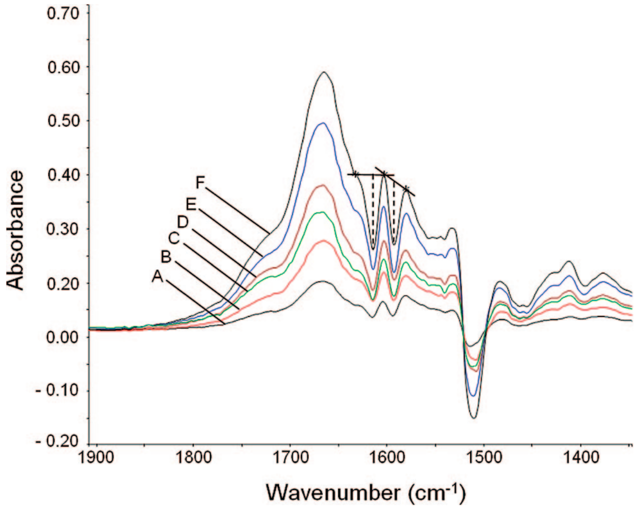

Figure 3. Difference spectra (i.e., spectrum at time t minus spectrum at time zero) obtained from the data of Figure 2B. Key: trace A, collection time, $t = 1.4 \times 10^3$ min; trace B, $t = 2.5 \times 10^3$ min; trace C, $t = 4.1 \times 10^3$ min; trace D, $t = 1.4 \times 10^4$ min; trace E, $t = 2.1 \times 10^4$ min; trace F, $t = 3.5 \times 10^4$ min.

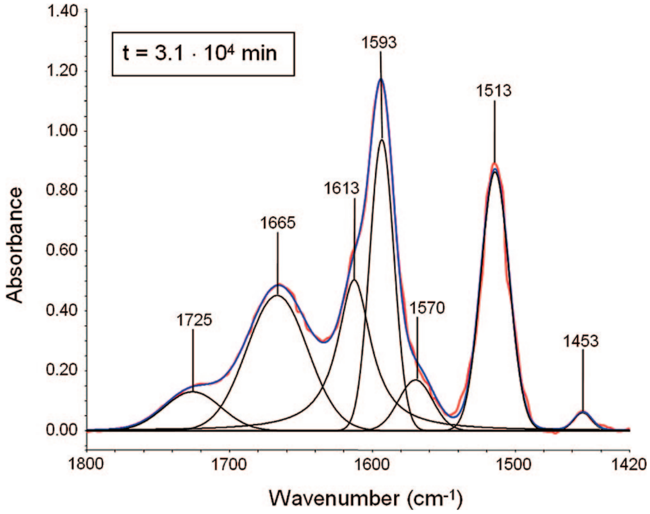

Figure 4. Curve fitting analysis in the wavenumber range 1800−1420 cm^{-1} of the spectrum collected after 3.1×10^4 min in the photodegradation experiment. The figure displays the experimental trace, the fitted profile, and the resolved components.

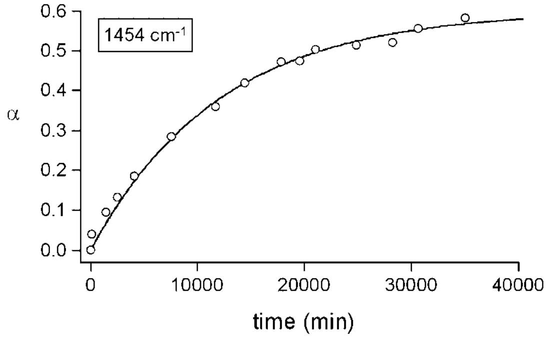

Figure 5. Relative conversion of the CH$_2$ groups as a function of photodegradation time. The empty circles represent experimental data, the continuous line is the kinetic profile obtained by the model in eq 3.

with respect to that at ν_j, and is negative otherwise. This holds true whenever the synchronous spectrum at ν_i,ν_j is positive; otherwise, the above relationship is reversed.

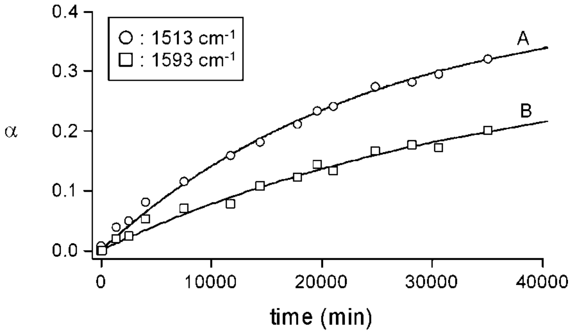

Figure 6. Relative conversion of the aromatic rings of the TGDDM unit (A) and of the DDS unit (B) as a function of photodegradation time. The empty circles and squares represent experimental data, the continuous lines are the kinetic profiles obtained by the model eq 3.

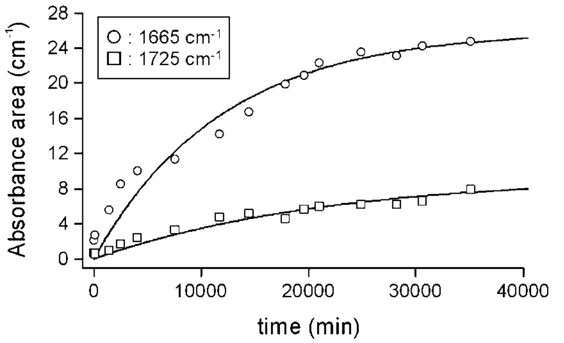

Figure 7. Absorbance area of the carbonyl peaks as a function of photodegradation time. The symbols represent data points, the lines are the kinetic profiles from model eq 5.

Table 1. Kinetic Constants and Final Conversions (or A_f) for the Various Functional Groups Involved in the Photo-Degradation Process

functional group	k (min^{-1} × 10^5)	α_f (%)	$\bar{\sigma}^{2\,c}$
CH_2	8.7 ± 0.6[a]	59 ± 1	0.016
Ar(TGDDM)	4.1 ± 0.1	42 ± 7	0.011
Ar(DDS)	2.7 ± 0.01	32 ± 5	0.010
C=O(amide)	8.9 ± 1	25 ± 1[b]	1.8
C=O(ketone)	4.6 ± 0.3	9.5 ± 0.5[b]	0.69

[a] SE (standard error of estimate). [b] A_f. [c] $\bar{\sigma}^2$ = mean standard deviation.

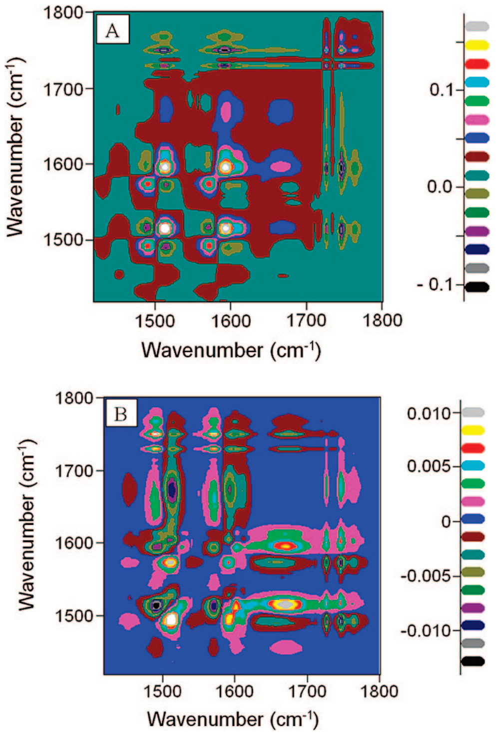

Figure 8. 2D-FTIR correlation spectra in the wavenumber range 1800−1420 cm^{-1}, for the TGDDM/DDS network subjected to photodegradation. Key: (A) synchronous spectrum; (B) asynchronous spectrum.

The most significant 2D-FTIR spectra are obtained in the region 1420 − 1800 cm^{-1}. These are reported in Figure 8A,B, while the results in terms of peaks' position, sign and relative intensity are summarized in Table 2A,B. In the region of the aromatic ring modes (below 1650 cm^{-1}) intense autopeaks are identified in the synchronous spectrum (Figure 8A) at [1492, 1492 cm^{-1}], [1515, 1515 cm^{-1}], [1573, 1573 cm^{-1}] and [1594, 1594 cm^{-1}], along with their respective cross-peaks at appropriate positions. With respect to the as-collected frequency spectra (see Figure 2B) the synchronous map highlights the components at 1573 and 1492 cm^{-1}, which, by careful inspection, can also be identified in the original profiles. In particular, the component at 1573 is clearly identified also by the LSCF analysis. The sign analysis reveals that the latter components increase in intensity with exposure time and, therefore, originate from reaction products, while the components at 1515 and 1594 cm^{-1} decrease (reagents). In fact, the cross-peaks at 1515−1492 and 1515−1573 cm^{-1}, as well as those at 1594−1492 and 1594−1573 cm^{-1} are negative, while those at 1573−1492 and 1594−1515 cm^{-1} are positive. At present, there is no evidence toward a unambiguous assignment of the 1573 cm^{-1} component to a specific molecular fragment. With respect to the signal at 1492 cm^{-1}, it may be noted that the TGDDM band originally centered at 1513 cm^{-1} is quite complex, indicating that the relative normal mode is very sensitive to the surrounding molecular environment. Accordingly, changes in the geometry (conformation) and/or substitution of the TGDDM aromatic ring may produce a structure absorbing preferentially at 1492 cm^{-1}, thus justifying the observed intensity increase. The IR peak at 1454 cm^{-1} yields a relatively modest autopeak due to its low intensity compared to those of the surrounding signals. It can be readily identified, however, along with its principal cross-peaks, by a suitable choice of the intensity scale.

The strongest improvement of resolution brought about by the 2D-FTIR analysis is seen in the carbonyl range (1660−1800 cm^{-1}). Here the amide band gives rise to a single autopeak at [1665, 1665 cm^{-1}] together with the associated correlations, while the carbonyl band at higher frequency is neatly resolved into three distinct components at [1728, 1728 cm^{-1}], [1748, 1748 cm^{-1}], and [1766, 1766 cm^{-1}]. The three autopeaks located above 1700 cm^{-1} display intense cross-correlations with each other; all of them display positive signs since all components increase with exposure time. Conversely, the cross-peaks relating the above components with the aromatic signals at 1573 and 1594 cm^{-1} are all negative, according to the fact that the intensity of the latter decreases with time. In summary, the synchronous map points to the existence of a single species absorbing at 1665 cm^{-1}, which can be identified as an N,N-disubstituted amide. Although 2D-FTIR analysis identifies only a single component, the formation of nonamidic carbonyls absorbing at a close frequencies, is to be considered. In particular, an acetophenone structure would produce a peak at 1684 cm^{-1}. On the basis of the available spectroscopic evidence, the occurrence of such a species under photo-oxidative conditions cannot be entirely ruled out.

The carbonyl band above 1700 cm^{-1} originates from the υ(C=O) modes of three distinct species. According to previous literature results,[16–21] and on the basis of group frequency considerations,[31,32] we may tentatively assign the component

Table 2. Peak Position, Sign and Relative Intensity for the Synchronous and Asynchronous Spectra in the Range 1420−1800 cm^{-1}

peak no.	position (cm^{-1})	sign	intensity (relative)	type[a]
		A. Syncronous		
1	1454−1454	+	w	A
2	1492−1492	+	s	A
3	1515−1515	+	s	A
4	1573−1573	+	s	A
5	1594−1594	+	s	A
6	1668−1668	+	s	A
7	1728−1728	+	s	A
8	1748−1748	+	s	A
9	1766−1766	+	w	A
10	1515−1492	−	w	C
11	1573−1492	+	s	C
12	1573−1515	−	w	C
13	1594−1515	+	s	C
14	1668−1594	+	m	C
15	1728−1594	−	m	C
16	1728−1515	−	m	C
17	1748−1728	−	m	C
18	1748−1594	−	m	C
19	1748−1515	−	m	C
20	1765−1748	+	m	C
21	1765−1728	+	m	C
22	1766−1594	−	vw	C
23	1765−1514	−	vw	C
		B. Asyncronous		
1	1513−1492	+	s	
2	1572−1513	−	s	
3	1593−1492	+	s	
4	1603−1513	+	s	
5	1603−1593	+	s	
6	1675−1514	+	s	
7	1675−1593	+	s	
8	1728−1492	−	m	
9	1728−1513	+	m	
10	1728−1572	−	m	
11	1728−1603	+	m	
12	1728−1675	+	m	
13	1748−1492	−	m	
14	1748−1515	+	m	
15	1748−1572	−	m	
16	1748−1602	−	m	
17	1748−1675	+	m	
18	1765−1492	−	w	
19	1765−1515	+	vw	
20	1765−1572	−	w	
21	1765−1675	+	vw	

[a] Type A: autopeak. Type C: cross-peak.

at 1728 cm^{-1} to a aldehyde structure of the following form:

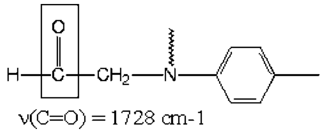

A ketonic group having the following structure

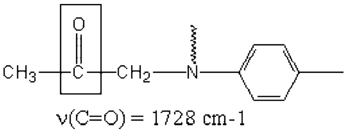

is also compatible with the observed peak position. Although the available spectroscopic evidence does not allow us to positively discriminate between the two, the aldehyde structure is to be preferred, insofar as this functional group absorbs about 15 cm^{-1} above the ketonic carbonyl. In fact, saturated aldehydes are quoted to absorb between 1740 and 1730 cm^{-1}, while saturated open-chain ketones lie in the frequency range 1720−1705 cm^{-1}.[30]

The absorption at 1748 cm^{-1} is likely to result from the presence of a substituent in close proximity to the carbonyl group which causes a blue shift of the relative stretching frequency. It is known that a polar group is effective in altering the υ(C=O) only if the substitution occurs not farther than at the α-carbon.[30,31] Furthermore, it has been established that the effect of oxygen substitution in the α-position is almost exactly coincident with that of chlorine substitution, causing a rise in the C=O frequency of about 20 cm^{-1}.[30] On the basis of the above considerations we associate the 1748 cm^{-1} component to an α-hydroxyl−aldehyde structure of the following form:

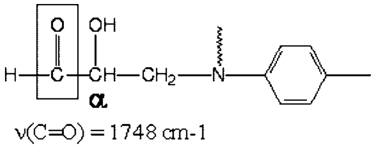

With respect to the component at 1766 cm^{-1}, it can be noted that few carbonyl groups absorb at such high frequency values. Among them there are the strained ring structures of the lactones, and in particular the five-membered ring, absorbing between 1760 and 1780 cm^{-1}. These structures have been actually detected as photo-oxidation byproduct in epoxy networks based on DGEBA/anhydride components,[10] but are unlikely to result from the present epoxy system. The υ(C=O) frequency of unsubstituted carboxylic acids is generally quoted between 1725 and 1700 cm^{-1}. These comparatively low values are however due to the effect of a strong H-bonding association (these compounds are usually found in dimeric form) which drives the carbonyl frequency downward. In the absence of such interaction, the carbonyl group experiences the same OH substituent effect just discussed for the case of the aldehyde, but stronger because the substitution occurs on the C=O carbon rather than on the α-carbon. Thus, it has been reported that a series of alkyl acids in diluted carbon tetrachloride solutions, i.e. in their monomeric form, absorb at an average frequency of 1760 cm^{-1}.[30,33] On the basis of the above considerations, we propose to assign the 1766 cm^{-1} component to an unassociated carboxylic acid structure of the form

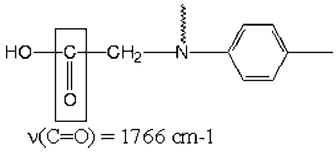

The fact that the carboxyl group is not involved in H-bonding interactions is reasonable in the light of the very low concentration of this species and because, according to the infrared results, in the present TGDDM/DDS system, most of the available proton-donors, i.e. the OH groups of the epoxy network, are already self-associated, forming a secondary network of H-bonding interactions.

In the asynchronous spectrum (Figure 8B) strong cross-correlation peaks are identified at [1513−1492 cm^{-1} (+)] and at [1593−1572 cm^{-1} (+)], corresponding to the components already detected in the synchronous spectrum. The most relevant features of the asynchronous map are those occurring in the carbonyl region. The presence of a single, broad component at 1675 is confirmed by the occurrence of distinct cross-peaks at [1675−1513 cm^{-1} (+)] and [1675−1593 cm^{-1} (+)]. The positive intensity of the above peaks indicates that the rate of formation of amide carbonyls is higher than the rate of depletion of aromatic groups, which, in turn, points to the occurrence of two distinct reaction pathways for the above processes, proceeding at different rates. The three carbonyl components identified above 1700 cm^{-1} in the synchronous map are confirmed by the appearance of characteristic patterns of asynchronous cross-correlations, along the vertical iso-frequency lines located at 1728, 1748, and 1766 cm^{-1}. In particular, the positive sign of the cross-correlations with the 1513 cm^{-1} component (i.e., at [1728−1513 cm^{-1} (+)], [1748−1513 (+)] and [1766−1513 (+)], taken together with the negative sign of the corresponding synchronous peaks, indicate that the carbonyl species absorbing in the present frequency range are produced at a faster rate than the aromatic groups are consumed. The same considerations apply to the cross-peaks involving the 1593 cm^{-1} component. Finally, the positive intensity of the cross-peaks at [1728−1675 cm^{-1} (+)], [1748−1675 (+)], and [1766−1675 (+)], and the negative sign of the corresponding synchronous peaks, indicate that amide groups are formed faster than the remaining carbonyl functionalities, as already apparent from the kinetic analysis discussed previously.

1.3. Proposed Photo-Oxidation Mechanism. Before entering into the details of the discussion, it is explicitly noted that the TGDDM component used throughout is a commercial grade product (see Experimental Section). Even if it contains a non-negligible amount of impurities, it is known that these arise mainly from oligomerization of the monomer during the synthesis. The oligomers do not introduce new functional groups, and hence, the molecular structure of the cured network is scarcely affected by these side reactions.

A mechanism to describe the photo-oxidative degradation of the TGDDM/DDS system has to account for the main findings of the spectroscopic analysis, which can be summarized as follows:

- The aliphatic part of the network is involved in the molecular breakdown process and is likely to represent the main site of initiation of the photo-oxidative process.
- The para-substituted aromatics of the TGDDM and the DDS units are both involved in a process which ultimately causes the loss of their aromatic character. In fact, any mechanism limited to the modification of the aromatic substitution would produce a frequency shift of the associated signals rather than the observed decrease of their intensity. Furthermore, the DDS unit is considerably more stable than the TGDDM unit.
- Photoinitiated oxidation of the epoxy network gives rise to a complex pattern of oxygenated species, among which amide groups, aldehyde/ketone functionalities and carboxylic acid groups have been tentatively identified by 2D-FTIR spectroscopy.

Concerning the initiation step, it has been shown that, in a wide variety of epoxy systems, irradiation in inert atmosphere leads to H_2 evolution, most likely due to the homolysis of CH bonds, which, therefore is to be considered an important primary event:[5,6]

$$PH \xrightarrow{hv} P^{\bullet} + H^{\bullet}$$

$$H^{\bullet} + PH \rightarrow P^{\bullet} + H_2$$

When oxygen is present, the primary macroradicals ($P^{\bullet}$) readily forms hydroperoxides, thus initiating the so-called basic autoxidation scheme (BAS).[34]

One possible reaction pathway starts by hydrogen abstraction on the methylene group linked to the nitrogen atom, as depicted in Scheme 1.

The resulting hydroperoxide group (structure II) evolves as usual, by thermal decomposition and formation of a peroxy-radical (structure III). Breaking at the N−C bond produces the aldehyde species detected spectroscopically (structure IV) and structure V, which is strongly stabilized by resonance.[9,11,16] In fact, Structure VI is a stable radical, which ultimately evolves through various paths, for example, by chain-transfer or O_2 combination to form a hydroperoxide. In any case, the aromatic character of the ring involved is lost, thus accounting for the decrease of the aromatic groups' concentration observed spectroscopically.

Scheme 2

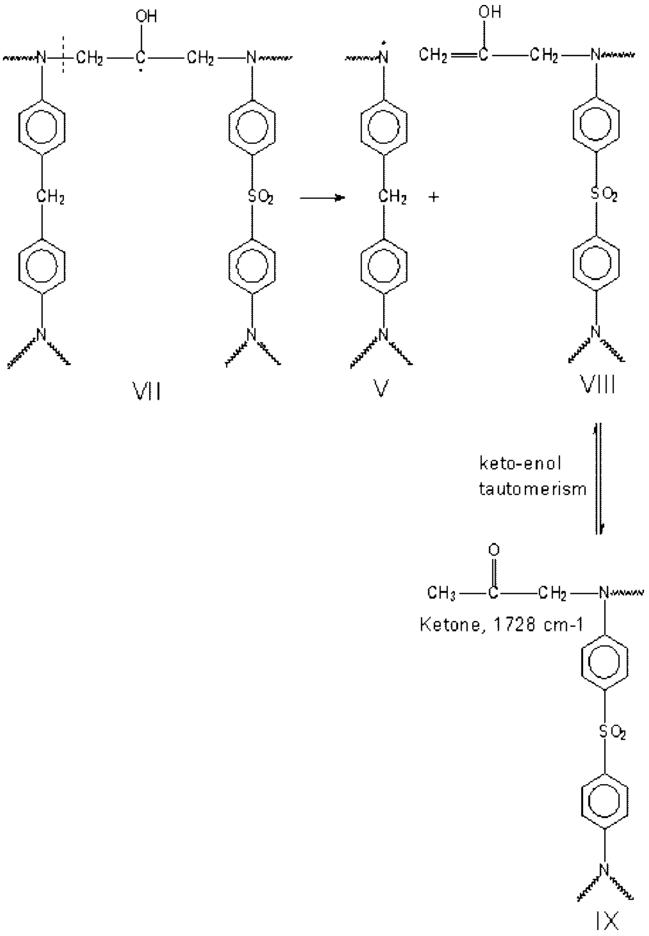

A concurrent degradation pathway may be envisaged (see Scheme 2) starting with hydrogen abstraction at the position:

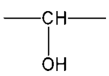

$$-\underset{\displaystyle OH}{\underset{|}{CH}}-$$

In this case the resulting structure VII evolves by β-scission forming structure V, already discussed in terms of resonance stabilization and further evolution, in scheme I. The other reaction product is an enol (VIII), which, by a keto−enol tautomerism gives rise to the ketonic structure IX, compatible with the carbonyl peak detected spectroscopically at 1728 cm^{-1}. It is worth noting the latter path is a photolysis process; i.e., it does not involve oxygen as reactant.

Structure VII may also evolve by oxygen attack via the hydroperoxide route, thus producing structure X, as depicted in Scheme 3.

Chain scission at the carbon−carbon bond produces a carboxylic acid (identified spectroscopically at 1765 cm^{-1}) and a hydroperoxide which ultimately would produce, by elimination of H_2O, an amide linkage (structure XIV, IR signal at 1675 cm^{-1}). However, this mechanism cannot be responsible for the whole production of amide groups in the system, insofar as the spectroscopic data demonstrate that the carboxylic acid concentration is very limited with respect to the other carbonyl

Scheme 3

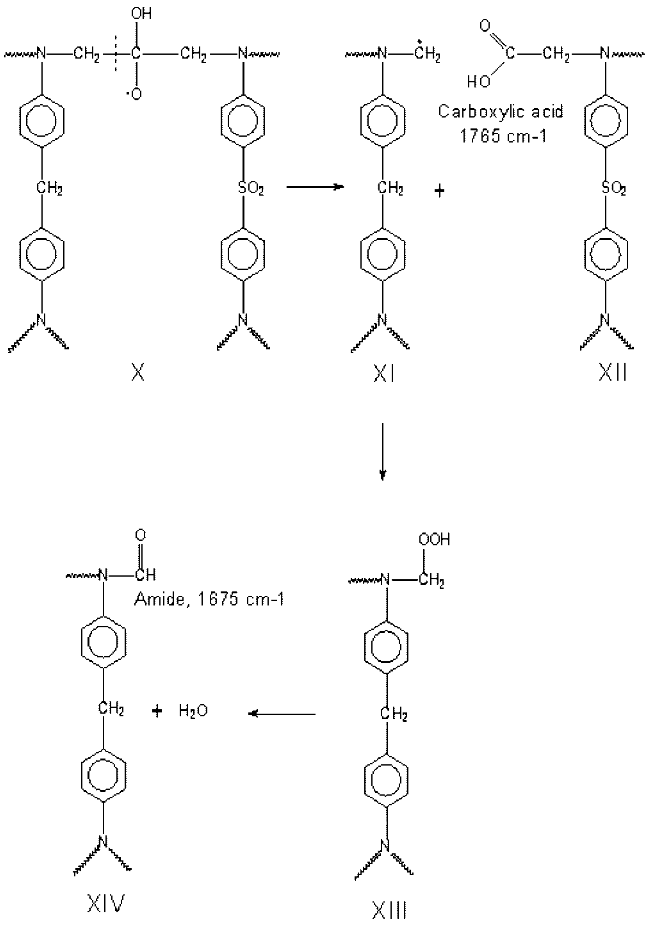

species, whereas the amide group concentration is strongly predominant.

It is inferred that the principal route for amide formation starts from the peroxy radical III of Scheme 1, with the chain-scission occurring at the carbon−carbon bond, rather than at the carbon−nitrogen bond (see Scheme 4). The mechanism ultimately produces a N−N disubstituted amide (structure XV) and a OH-terminated macroradical (structure XVI), which may propagate the photo-oxidative sequence by hydrogen abstraction, thus forming alcoholic moieties not readily detected by IR spectroscopy because of the presence of a conspicuous amount of hydroxyl groups within the network.

The latter route is to be considered predominant among those discussed so far in view of the higher reaction rate for the amide group formation with respect to those of the other carbonyl species, as evidenced by the kinetic analysis. The above mechanism also justifies the significantly higher rate of formation of amide groups with respect to the rate of depletion of the aromatic rings. In fact these two processes occur through independent and competitive reaction pathways.

The photo-oxidative mechanisms outlined above do not account for the significantly higher stability of the aromatic rings of the DDS unit with respect to those of the TGDDM unit. In fact, owing to the symmetry of the aliphatic segment of the network around the CH−OH group, the reaction paths have the same chance to proceed toward the TGDDM or the DDS side. An analogous effect was observed in the case of thermal-degradation of the TGDDM/DDS network,[16,17,21] and was explained by assuming an alternative path starting with the hydrogen abstraction from the methylene group linked to the aromatics in the TGDDM unit, which is absent in the DDS unit (Scheme 5).

Scheme 4

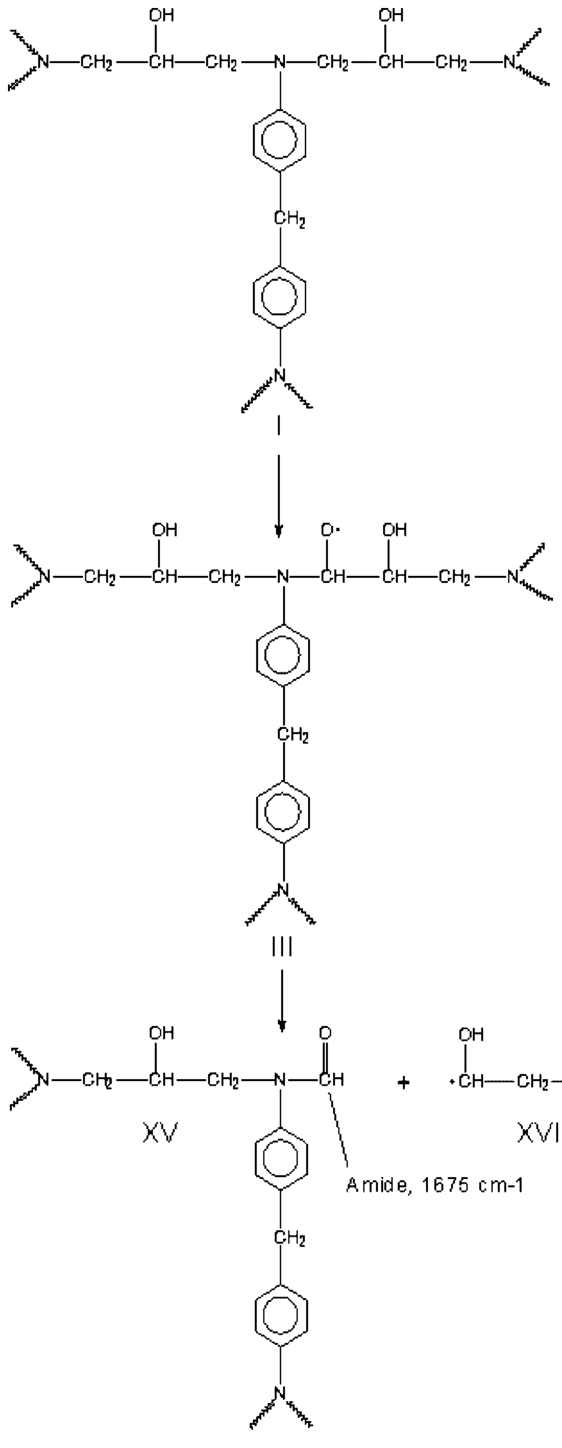

Structure XVII, is a stable radical similar to structure VI and may evolve accordingly, with the disruption of the aromatic character of the TGDDM ring and the formation of conjugated structures responsible for the darkening of the sample after both irradiation and thermal degradation.

In summary, the photo-oxidative degradation of the TGDDM/DDS network is a complex process involving several mechanisms which ultimately bring about chain-scission mainly localized on the aliphatic segment of the network. These molecular processes are responsible for the lowering of the overall cross-link density of the network, with consequent reduction of T_g. More on this in the paragraph dealing with the dynamic-mechanical analysis. The mechanisms which are more likely to occur have been proposed: two main photo-oxidative

Scheme 5

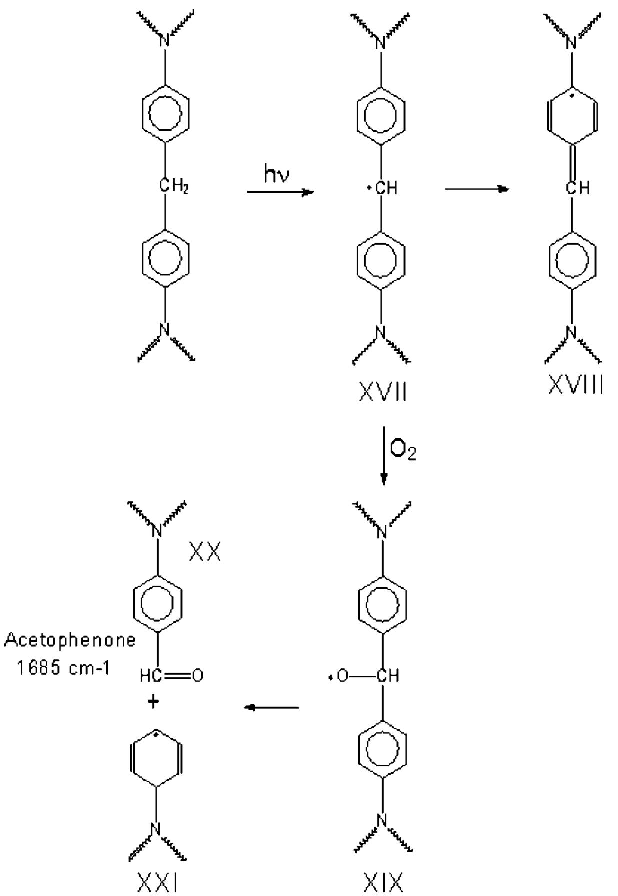

routes can be identified (possibly competitive) leading, respectively, to amide and carbonyl groups. According to the kinetic analysis and to the results of 2D-FTIR correlation spectroscopy, the amide route is largely prevailing under photo-oxidative conditions.

2. Dynamic Mechanical Analysis. Dynamic−mechanical spectra in terms of storage modulus (E') and tan δ at 1 Hz for the plain TGDDM/DDS resin and for the same resin photo-oxidized for 600 and 1000 h are shown in Figure 9a−c. The tan δ plots reveal the occurrence of three distinct relaxation processes at increasing temperatures. In particular, the relaxation at the lowest temperature (Figure 9b) is generally denoted as the β transition and is associated to localized motions of small units of the epoxy network, while the relaxation appearing in the highest temperature region (Figure 9c) is an α-transition process and corresponds to the T_g. In fact, in this region the storage modulus (Figure 9a) shows a sharp drop and then approaches a constant value (rubbery plateau). The relaxation process between the α and β peaks is denoted as ω; its molecular origin is still uncertain.[35−37]

The data of Figure 9 show clearly the changes induced by the photo-oxidative process, which can be summarized as follows:

(i) The modulus in the rubbery region decreases markedly with increasing the exposure time. (ii) The intensity of β, ω, and α transitions also decreases. (iii) The α and β relaxation peaks (T_g and T_β) are shifted to lower temperatures as the exposure time increases, while the position of the ω relaxation peak (T_ω) remains essentially unchanged after 600 h. Subsequently, at 1000 h, this transition becomes barely detectable, and a new relaxation, indicated as α′, appears in the range 140−200 °C as a shoulder of the principal peak.

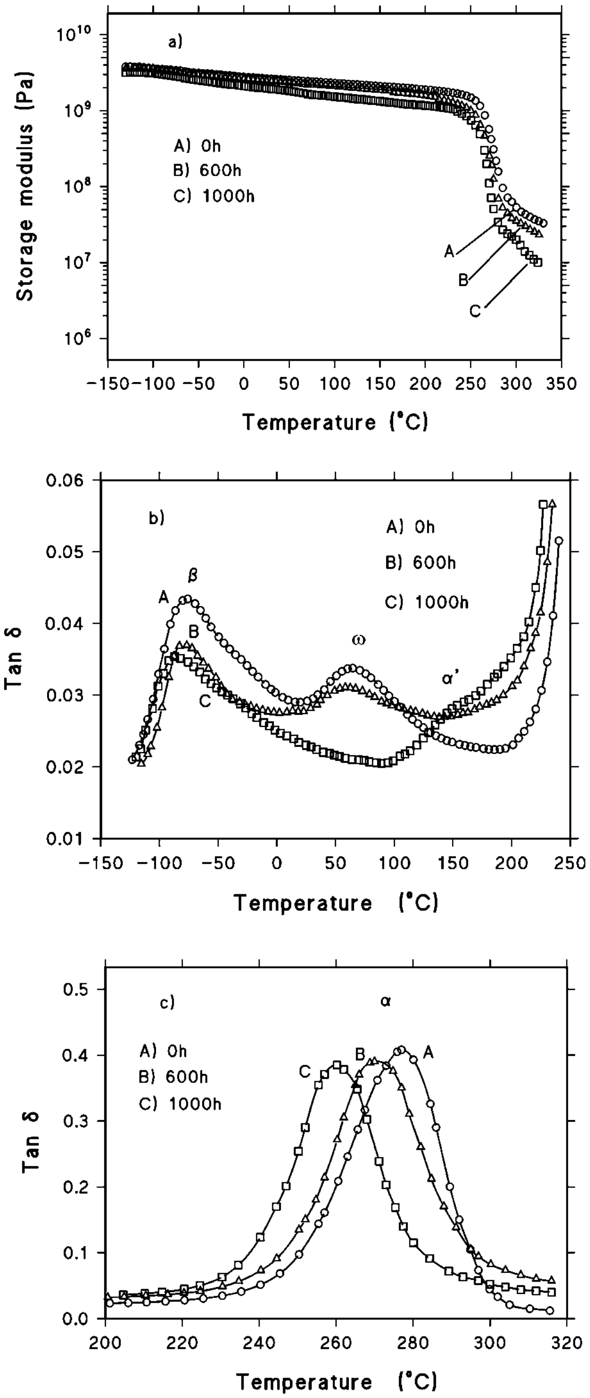

Figure 9. (a) Storage modulus (E') as a function of temperature for TGDDM/DDS resins before and after photo-oxidation. Exposure time as indicated. (b) Loss factor (tan δ) as function of temperature in the range −150 to +250 °C for TGDDM/DDS resins before and after photo-oxidation. Exposure time as indicated. (c)) Loss factor (tan δ) as function of temperature in the range 200−320 °C for TGDDM/DDS resins before and after photo-oxidation. Exposure time is as indicated.

In Table 3 are reported the values of T_β, T_ω, and T_g determined from the maxima of the tan δ curves. It can be seen that for the two photo-oxidized samples the decrease in T_g is, respectively, 8 and 18 °C, whereas for the T_β the reduction is of about 6 and 10 °C.

It is known that in highly cross-linked networks the peak position and the intensity of the primary and secondary relaxation processes are related to the cross-link density.[35−37] Thus, the rubber elasticity theory along with the experimental

Table 3. Transition Temperatures (T_β, T_ω, T_g), Rubbery Modulus (E_r), M_c, and Cross-Link Density (ν_e) of TGDDM/DDS Resins before and after Photo-Oxidation

sample	exposure time (h)	T_β (°C)	T_ω (°C)	T_α (°C)	E'_r (Pa)	M_c (g/mol)	ν_e (mol cm^{-3})
TGDDM/DDS	0	−72.2	62.4	278.0	4.0×10^7	463.2	2.7×10^{-3}
TGDDM/DDS	600	−78.1	61.5	270.0	3.1×10^7	589.5	2.1×10^{-3}
TGDDM/DDS	1000	−82.2		260.0	2.0×10^7	928.1	1.4×10^{-3}

Scheme 6

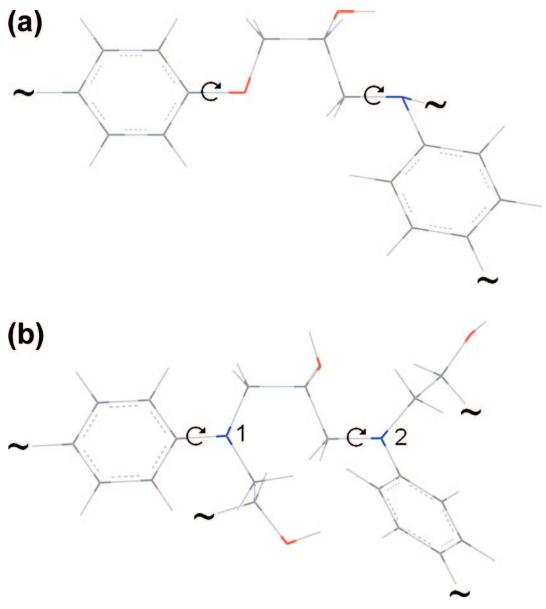

storage modulus in the rubbery region were used to estimate the cross-link density of the neat and photo-oxidized epoxy networks through the following relationship:[41–43]

$$M_c = 3\rho RT/E_r \tag{6}$$

Here M_c is the average molecular weight between two cross-link points, ρ is the density of the network at the absolute temperature T, R is the gas constant, and E_r is the rubbery modulus, defined in this study as the value of E' at 40 °C above its α relaxation peak.

The M_c values calculated by applying this method together with the cross-link density, evaluated from the relationship $\nu_e = \rho/M_c$,[35] are reported in Table 3. It is found that M_c increases and decreases as the photo-oxidation time increases. In particular, ν_e decreases as the photo-oxidation time increases. In particular, ν_e decreases by 22.2% and 48.1% with respect to the original network. This decrease accounts for the marked lowering of the glass transition temperature and, at the same time, indicates that a massive chain scission takes place during the photo-oxidation process.

In the light of the spectroscopic results, the chain scission processes mainly responsible of the above effect can be identified as those occurring within the aliphatic segment of the network and, in particular, at the carbon−carbon bond (see Scheme 4). Obviously, other mechanisms contribute, as those outlined in Schemes 1, 2 and 3.

With respect to the β transition, the dynamic-mechanical analysis evidences that, in terms of peak shift, the effect of photoaging is lower than that on the α transition. In order to account for this result, we have to take into consideration the molecular origin of the β transition. Several literature studies have attributed the above relaxation to a crankshaft rotation motion of the glycidyl portion of the epoxide group in TGDDM after reaction with DDS.[44–46] This interpretation was essentially based on an analogy with the behavior of bifunctional epoxy networks (DGEBA/DDS). However, there are two considerations against the above assignment: first of all the crankshaft motion is feasible, in principle, in DGEBA based networks where the $-CH_2-CHOH-CH_2-$ segment is linked to an oxygen and a nitrogen atom thus allowing the simultaneous rotation of two CH_2- bonds (Scheme 6a). In the case of the TGDDM based structure the $CH_2-CHOH-CH_2-$ segment is linked to two nitrogen atoms (Scheme 6b).

Only the bond with the nitrogen labeled 2 can rotate freely, while the rotation of the bond with nitrogen labeled 1 is hindered, with the latter being a cross-link point. A second argument arises from the consideration that, if the segment involved in the β relaxation were that reported in Scheme 6b, according to the spectroscopic results, a much extensive effect of photoaging, similar to that found for the α transition, would have resulted. We propose to associate the β peak to the rotation of the disubstituted phenyl rings. This interpretation is supported by the value of activation energy we have estimated for the transition (to be discussed later) and justifies the lower effect of photoaging, insofar as the degradation mechanisms which produce the disruption of the aromatic rings (i.e., Schemes 1, 2 and 5) are to be considered minor reaction pathways.

As far as the ω relaxation is concerned, it has not received great attention in the literature. It has been generally attributed to the local motion of chain segments heavily restricted by cross-

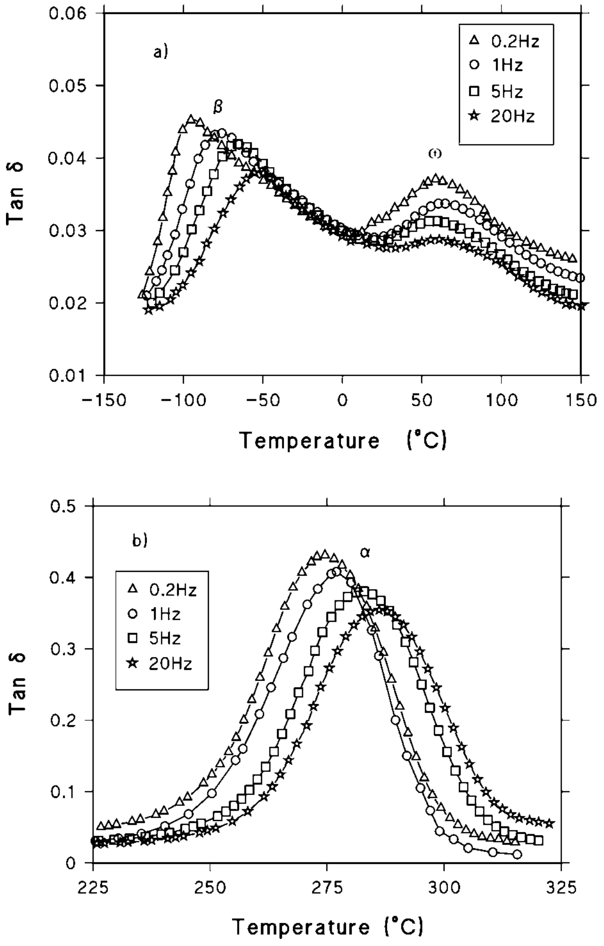

Figure 10. Loss factor (tan δ) as function of temperature for the control TGDDM/DDS resin, at different frequencies: (a) temperature range −150 to +150 °C; (b) temperature range 225 to 325 °C.

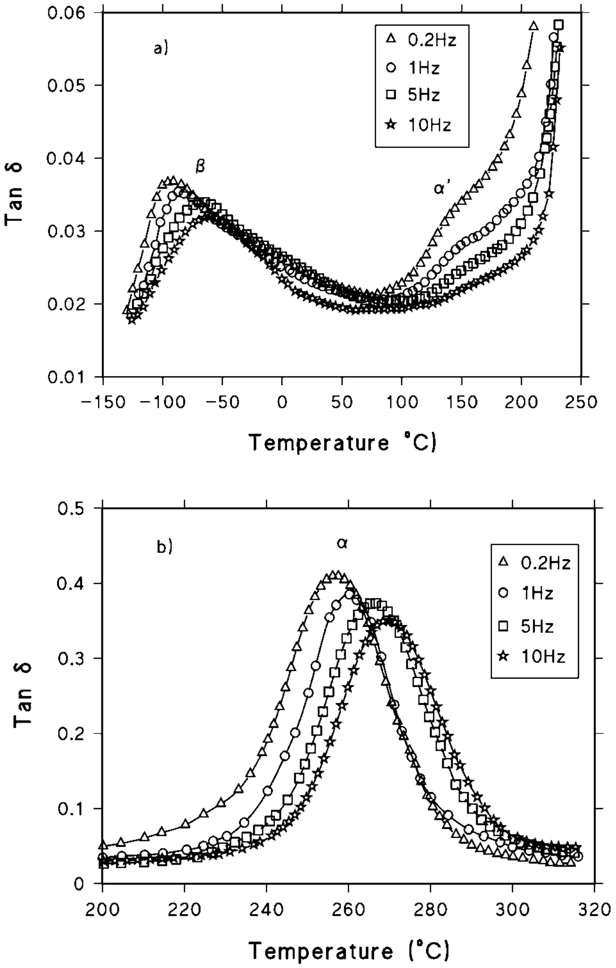

Figure 11. Loss factor (tan δ) as function of temperature for the TGDDM/DDS resin photo-oxidized for 1000 h, at different frequencies: (a) temperature range −150 to +150 °C; (b) temperature range 225 to 325 °C.

linking points.[47–50] Upon degradation (1000 h) the vanishing of the transition can be attributed to the chain-scission which reduces these cross-linking points. The appearance of the α′ relaxation is to be related to more cooperative mechanisms involving newly formed dangling chains.

Further details on the effect of the photo-oxidation on the relaxation processes were gathered by a multifrequency analysis, which was performed at nine frequencies from 0.05 to 20 Hz.

In Figure 10 and 11 are shown the tan δ versus temperature curves, collected at different frequencies, for the as-prepared resin (Figure 10, parts a and b) and for the resin photo-oxidized for 1000 h (Figure 11, parts a and b). It is found that, by increasing frequency, the intensities of transitions decrease and the peak maxima shift at higher temperatures. The latter effect is more pronounced for the β transition, followed by the α, while the ω and α′ relaxations display a much lower sensitivity.

The dependence of β and α transitions on frequency has been examined using the Arrhenius equation

$$f = A\exp(-E_a/RT) \quad (7)$$

where f is the frequency, A is the pre-exponential factor and E_a is the activation energy.

The above equation is generally suitable for noncooperative processes (i.e., sub-T_g transitions). For long-range motions (α transitions) the method remains suitable if applied within a relatively narrow range of frequencies (2 or 3 orders of magnitude), although the E_a so obtained represents a limiting or apparent value.

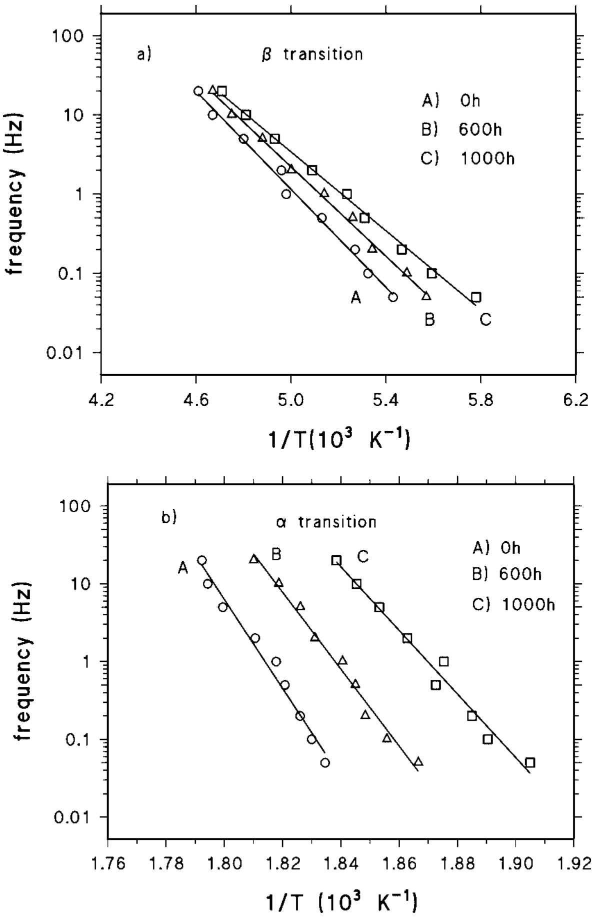

Figure 12. Arrhenius plot relative to the β transition for TGDDM/DDS resins before and after photo-oxidation. Exposure time as indicated. (b) Arrhenius plot relative to the α transition for TGDDM/DDS resins before and after photo-oxidation. Exposure time as indicated.

Table 4. Activation Energy ($E_{a,\beta}$, $E_{a,\alpha}$) and Activation Entropy (ΔS^+) of TGDDM/DDS Resins before and after Photo-Oxidation

sample	exposure time (h)	$E_{a,\beta}$[a] (kJ/mol)	$E_{a,\alpha}$ (kJ/mol)	$E_{a,\beta}$[b] (kJ/mol)	ΔS^+ (J mol^{-1} K^{-1})
TGDDM/DDS	0	59.2	1090	47.1	60.3
TGDDM/DDS	600	54.2	930	45.8	42.8
TGDDM/DDS	1000	46.1	775	44.6	7.8

[a] From the multifrequency analysis. [b] From the Starkweather method.

From Eq. 7 the activation energies of the β and α relaxation processes were evaluated as shown in Figure 12, where the logarithm of frequency is plotted versus *1/T*. The $E_{a,\beta}$ and $E_{a,\alpha}$ values determined from the slope of the Arrhenius plots are summarized in Table 4. For the resin exposed for 600 h, the values differ slightly from those of the control resin, while a significant reduction is found for the resin exposed for 1000 h. This lowering of activation energies is due to the photo-oxidation which, as a result of chain scissions, increases the molecular mobility of the chain segments and/or decreases the cooperative character of the relaxation processes involved. A more quantitative analysis of the cooperative effects was attempted for the β relaxation by considering the activation energy as a free energy term and evaluating the enthalpic (ΔH^+) and entropic (ΔS^+) contributions as proposed by Starkwether.[51,52] In such a description, the relationship between frequency and temperature can be expressed by the following equation:[53,54]

$$f = (kT/2\pi h)\exp(\Delta H^+/RT)\exp(\Delta S^+/R) \quad (8)$$

where k and h are, respectively, the Boltzman and Plack constants.

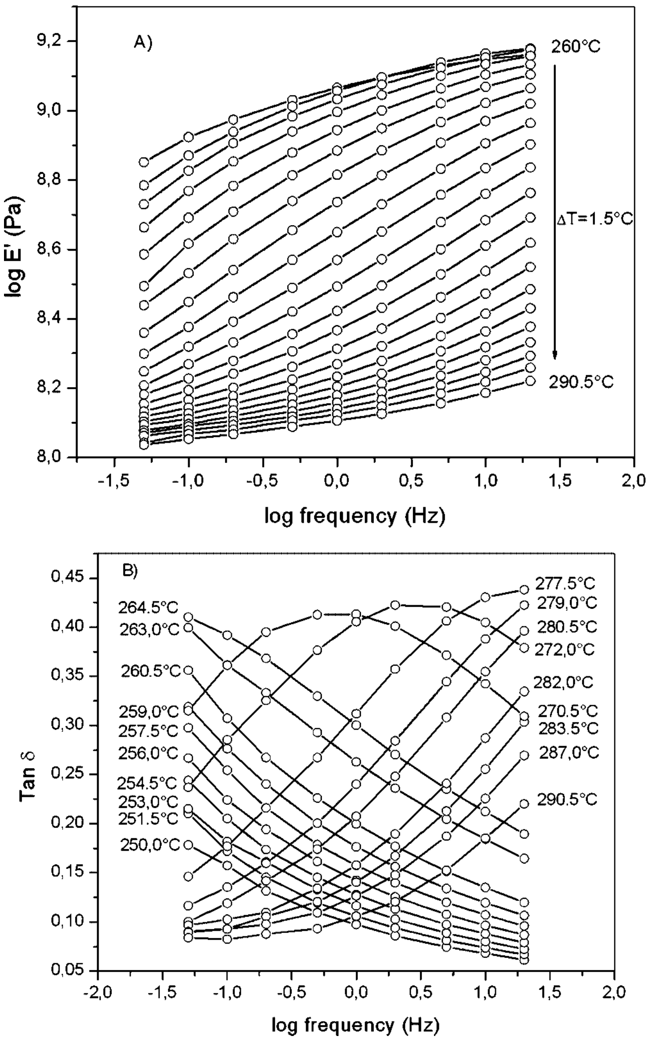

Figure 13. (A) Storage modulus (E') isotherms as a function of frequency in the range 0.05 to 20 Hz for the TGDDM/DDS resin photo-oxidized for 1000 h. (B) Loss factor (tan δ) isotherms in the range 0.05−20 Hz for the TGDDM/DDS resin photo-oxidized for 1000 h.

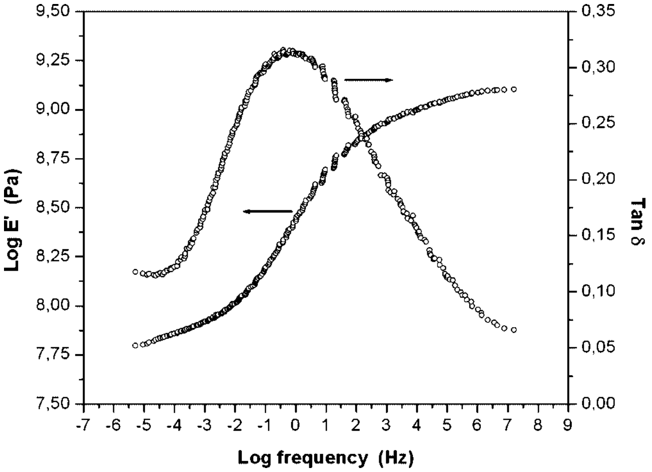

Figure 14. Master curves for the storage modulus (E') and loss factor (tan δ) relative to the TGDDM/DDS resin photo-oxidized for 1000 h.

The relation between the activation energy and the activation enthalpy is given by

$$E_a = \Delta H^+ + RT \tag{9}$$

in eq 9 the Arrhenius activation energy is

$$E_a = R\frac{d(\ln f)}{d(1/T)} \tag{10}$$

and the Eyring activation enthalpy is

$$\Delta H^+ = R\frac{d(\ln f)}{d(1/T)} \tag{11}$$

Combining eqs 8 and 9, we obtain

$$E_a = RT[1 + \ln(k/2\pi h) + \ln(T/f) + T\Delta S^+] \tag{12}$$

Starkweather found that for relaxation processes involving the motion of small segments, the activation entropy is close to zero. Under this assumption the activation energy follows a simple, linear dependence with temperature

$$E_a = RT'\,[1 + \ln(k/2\pi h) + \ln T'] \tag{13}$$

where T' is the temperature of the maximum of the β peak observed at 1 Hz.

The difference between the experimental activation energy and this theoretical value is equal to $T\Delta S^+$. Thus eq 13 defines an effective lower limit for the activation energies of viscoelastic processes below T_g. In Table 4 are collected the activation energies, derived from the Starkweather analysis and the values of ΔS^+. It can be noted that for the neat resin the activation energy differs significantly from that calculated experimentally, and the value of ΔS^+ is higher than zero. These results denote that the β transition is not fully localized on the phenyl groups, as proposed previously but retains a limited cooperative nature, in agreement with the literature results.[55,56] It is to be recalled, however, that, according to Starkweather, ΔS^+ values up to 100 J mol^{-1} K^{-1} are still to be considered noncooperative. The data of Table 4 also show that ΔS^+ decreases with increasing the photo-oxidation time. Thus, the photo-oxidation makes the β transition fully localized.

The dynamic−mechanical data, obtained by multifrequency experiments as a function of temperature, were also used to assess the viscoelastic parameters in the glass transition region of the photo-oxidized networks in comparison to those of the parent resin. As an example of this calculation, in Figure 13 are illustrated, for the resin photo-oxidized for 1000 h, the isotherms of E' (Figure 13A) and tan δ (Figure 13B) as a function of frequency in the temperature range from T_g − 30 °C to T_g + 30 °C. According to the time (frequency)−temperature superposition principle,[57,58] these curves can be shifted along the frequency axis to produce master curves over an extended frequency range at a reference temperature T_0.[58] In principle, a

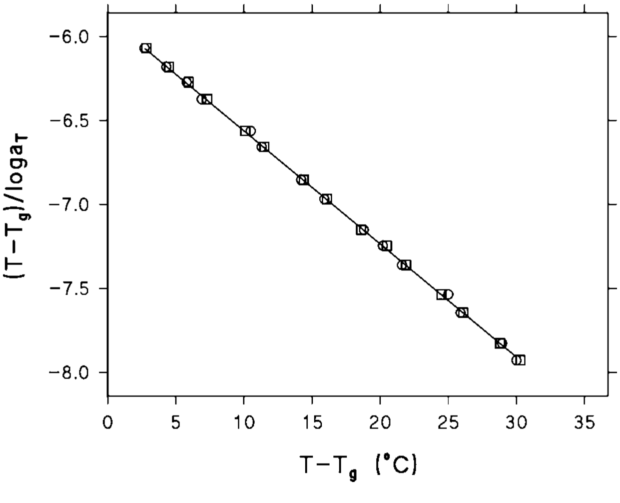

Figure 15. Evaluation of the viscoelastic parameters C_1^g and C_2^g from the shift factors of the master curves E' (○) and tan δ (□) for the TGDDM/DDS resin photo-oxidized for 1000 h.

Table 5. Viscoelastic Parameters of TGDDM/DDS Resins before and after Photo-Oxidation

sample	exposure time (h)	C_1^g (°C)	C_2^g (°C)	$C_1^gC_2^g$ (°C)	$f_g/B \times 10^2$	$\alpha_f/B \times 10^3$
TGDDM/DDS	0	18.6	88.8	1651.7	2.33	0.263
TGDDM/DDS	600	17.4	88.1	1532.9	2.49	0.284
TGDDM/DDS	1000	14.7	86.9	1277.4	2.96	0.340

vertical shift should also to be applied to account for the variation in polymer density between T and T_0. In the present case this correction is negligible due to the narrow temperature range considered. Therefore, master curves were build up without considering any vertical shift. In Figure 14 are shown the master curves obtained from Figure 13, parts A and B, in which the T_g at 1 Hz was taken as reference temperature.

In the glass transition region, the temperature dependence of the shift factor, a_T, follows the well-known Williams–Landel–Ferry (WLF) equation[57,58]

$$\log a_T = -\frac{C_1^g(T - T_0)}{C_2^g + T - T_0} \tag{14}$$

where C_1^g and C_2^g are the values of the viscoelastic coefficients at T_g.

According to Eq. 14, C_1^g and C_2^g can be obtained by plotting $(T - T_g)/\log a_T$ versus $(T - T_g)$. As illustrated in Figure 15, the values of a_T, deduced from E' and tan δ curves, give a unique straight line, indicating that the viscoelastic behavior of the photo-oxidized resin follows the time–temperature superposition principle. The parameters C_1^g and C_2^g evaluated from the slope and the intercept of the straight-line of Figure 15 are reported in Table 5 along with the same values relative to the sample aged for 600 h and to the parent resin. For the reference resin the values of C_1^g and C_2^g are close to those we found in a previous work[59] for TGDDM/anhydride networks, and are in agreement with the few values available in the literature.[60] The photo-oxidation decreases both C_1^g and C_2^g. Even if this reduction is rather limited, it can give important information about the network structure, since C_1^g and C_2^g are related to molecular quantities through the following equations:

$$C_1^g = B/2.3f_g \quad \text{and} \quad C_2^g = f_g/\alpha_f \tag{15}$$

Here f_g is the free volume fraction at T_g, α_f is the thermal expansion coefficient of the free volume and B is an empirical constant generally assumed to be equal to unity.[55,61]

Values of f_g/B and α_f/B evaluated from eq 15 are reported in Table 5. It can be observed that both f_g/B and α_f/B increase with increasing the exposure time. This effect is more significant for the resin photo-oxidized for 1000 h. The above results can be rationalized by considering that the chain-scission reactions occurring in the photo-oxidation process reduce the cross-links density, thereby enhancing the free volume and the tendency of the system to undergo thermal expansion.

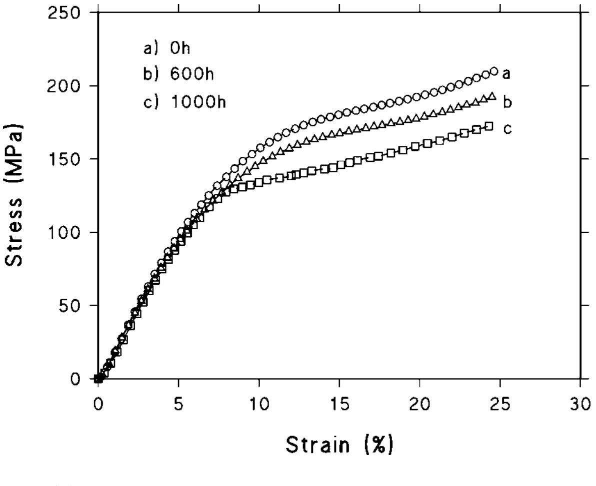

Figure 16. Stress–strain curves for TGDDM/DDS resins before and after photo-oxidation. Exposure time is as indicated.

Table 6. Mechanical Properties of TGDDM/DDS Resins before and after Photo-Oxidation

sample	exposure time (h)	compressive modulus (GPa)	compressive yield strength (MPa)	strain at yield (%)
TGDDM/DDS	0	3.2	179	15.1
TGDDM/DDS	600	3.1	160	13.4
TGDDM/DDS	1000	3.0	135	11.3

3. Mechanical Properties. In order to study the influence of the photo-oxidation on the plastic behavior of the epoxy network, mechanical tests under uniaxial compressive mode were performed. In Figure 16 are shown the stress–strain curves of neat and photo-oxidized samples, obtained at ambient temperature and at a rate of deformation of 1 mm/min. It can be seen that, for all the samples, the compressive deformation involves extensive yielding and strain hardening. For convenience, the stress–strain curves have been reported up to 25% deformation, although the samples were found to deform to strains exceeding 30%.

In the elastic region, the curves are almost coincident, indicating that the photo-oxidation scarcely affect the elastic properties such as the Young's modulus (see also Table 6). Indeed, the neat and the photo-oxidized resins have comparable moduli, showing that this parameter is mainly dependent on the interaction between chains rather than on the cross-link density. On the other hand, significant differences are displayed in the high-strain region where the yielding process occurs. In fact, the compressive yield strength, estimated as the stress corresponding to 5% offset from the elastic strain, decreases as the photo-oxidation time increases and is reached at lower deformations (Table 6). The yield strength, as opposed to modulus, is a high-strain property, and therefore is dependent on the cross-link density. Considering that the yielding is an energy activated process[62,63] involving movements of molecular segments in the direction of the applied stress, the results of Table 6 indicate that the chain scission reactions lower the energy barrier for yielding to occur, allowing it to take place at lower stress and stain values.

Concluding Remarks

FTIR spectroscopy has allowed us to simultaneously monitor the photodegradation of several groups present on a TGDDM/DDS network, so as to rank their relative stability. It was concluded that the aliphatic segment is the more susceptible to degradation, with initiation occurring at the methylene group. The aromatic moieties also undergo degradation, albeit at a lower rate, with the aromatics of the DDS unit being more stable than those of the TGDDM unit. Among the various carbonyl groups formed by photo-oxidation, 2D-FTIR spectroscopy identified N-substituted amides, aldehyde/ketone functionalities and carboxylic acids as minor component. The kinetic analysis demonstrated that all concentration profiles can be suitably described by a phase-boundary model with reaction order equal to one, thus allowing to evaluate the kinetic constants for the main functional groups involved in the process. On the basis of the spectroscopic results the most likely photodegradation mechanisms have been proposed and discussed.

A dynamic-mechanical analysis was performed to gain an insight in the effect of chain-scission reactions on the viscoelastic properties of the material. Marked reduction of the rubbery modulus, the primary and secondary relaxation temperatures and the intensity of all relaxation peaks were found upon photodegradation. These effects were discussed and interpreted in the light of the proposed degradation mechanisms. The results have also allowed to propose a more likely interpretation of the molecular origin of the β relaxation with respect to those reported in the literature. A viscoelastic analysis in terms of the WLF approach showed that the free volume and the thermal expansion coefficient of the network increase with degradation time, as a consequence of the chain-scission reactions. The compressive mechanical test showed a marked reduction of the mechanical performances of the material at high exposure times, especially in terms of yield—stress and strain.

References and Notes

(1) Lee, H.; Neville, K. *Handbook of Epoxy Resins*; McGraw-Hill: New York, 1990.
(2) Gillham, J. K. *Encyclopedia of Polymer Science and Technology,* 2nd ed.; John Wiley: New York, 1986; pp 519−524.
(3) May, C. A. *Epoxy Resins, Chemistry and Technology*, 2nd ed.; Marcel Dekker Inc.: New York, 1988.
(4) Ellis, B. *Chemistry and Technology of Epoxy Resins*; Blackie Academic and Professional: Glasgow, Scotland, 1993.
(5) Devanne, T.; Bry, A.; Audouin, L.; Verdu, J. *Polymer* **2005**, *46*, 229.
(6) Devanne, T.; Bry, A.; Raguin, N.; Sebban, M.; Palmas, P.; Audouin, L.; Verdu, J. *Polymer* **2005**, *46*, 237.
(7) Bellenger, V.; Verdu, J. *J. Appl. Polym. Sci.* **1985**, *30*, 363.
(8) Bellenger, V.; Verdu, J. *J. Appl. Polym. Sci.* **1983**, *28*, 2599.
(9) Bellenger, V.; Verdu, J. *J. Appl. Polym. Sci.* **1983**, *28*, 2677.
(10) Ollier-Dureault, V.; Gosse, B. *J. Appl. Polym. Sci.* **1998**, *70*, 1221.
(11) Zhang, G; Pitt, W. G.; Goates, S. R.; Owen, N. L. *J. Appl. Polym. Sci.* **1994**, *54*, 419.
(12) Monney, L.; Belali, R.; Vebrel, J.; Dubois, C.; Chambaudet, A. *Polym. Degrad. Stab.* **1998**, *62*, 353.
(13) Dubois, C.; Monney, L.; Bonnet, A.; Chambaudet, A. *Composites* **1999**, *30*, 361.
(14) Mailhot, B.; Morlat-Therias, S.; Ouahioune, M.; Gardette, J. L. *Macromol. Chem. Phys.* **2005**, *206*, 575.
(15) Mailhot, B.; Morlat-Therias, S.; Bussiere, P. O.; Gardette, J. L. *Macromol. Chem. Phys.* **2005**, *206*, 585.
(16) Musto, P.; Ragosta, G.; Russo, P.; Mascia, L. *Macromol. Chem. Phys.* **2001**, *202*, 3445.
(17) Musto, P. *Macromolecules* **2003**, *36*, 3210.
(18) Marquardt, D. W. J. *Soc. Ind. Appl. Math.* **1963**, *11*, 441.
(19) Maddams, W. F. *Appl. Spectrosc.* **1980**, *34*, 245.
(20) Noda, I. *Appl. Spectrosc.* **2003**, *57*, 1094.
(21) Musto P. Ph.D. Thesis, Epoxy-Bismaleimide Systems: Network Development and Structure, University of Loughborough, U.K., **2000**.
(22) Levchic, S. V.; Camino, G.; Luda, M. P.; Costa, L.; Muller, G.; Costes, B. *Polym. Degrad. Stab.* **1998**, *60*, 169.
(23) Rose, N.; Le Bras, M.; Bourbigot, S.; Delobel, R.; Costes, B. *Polym. Degrad. Stab.* **1996**, *54*, 355.
(24) Venger, A. E.; Fraiman, Y. E.; Yurevic, F. B. *J. Therm. Anal.* **1983**, *27*, 325.
(25) Noda, I.; Ozaki, Y. *Two-Dimensional Correlation Spectroscopy*; Wiley: Chichester, U.K., 2004.
(26) Noda, I. *Appl. Spectrosc.* **1993**, *47*, 1329.
(27) Ozaki, Y.; Liu, Y.; Noda, I. *Appl. Spectrosc.* **2000**, *54*, 526.
(28) Sasic, S.; Zhang, J.; Ozaki, Y. *Vibr. Spectrosc.* **2007**, *44*, 50.
(29) Wu, P.; Siesler, H. W. *J. Mol. Struct.* **2000**, *521*, 37.
(30) Bellamy L. J., *The Infrared Spectra of Complex Molecules*; Chapman and Hall: New York, 1975; Vol. *1*.
(31) Colthup N. B.; Daly, L. H.; Wiberley, S. E. *Introduction to Infrared and Raman Spectroscopy*; Academic Press, San Diego, CA, 1990.
(32) Roeges N. P. G. *A Guide to the Complete Interpretation of Infrared Spectra of Organic Structures*; Wiley: New York, 1994.
(33) Grove, B.; Willis, J. *J. Chem. Soc.* **1951**, 887.
(34) Kelen, T. *Polymer Degradation*; Van Nostrand: New York, 1983.
(35) Sasuga, T.; Udagawa, A. *Polymer* **1991**, *32*, 402.
(36) Mikalajczak, G.; Cavaille, J. Y.; Johari, G. P. *Polymer* **1987**, *28*, 2023.
(37) Vignoud, L.; David, L; Sixou, B; Vigier, G *Polymer* **2001**, *42*, 4657.
(38) Chung, H. L.; Kenneth, A. H.; William, W. W. *Br. Polym. J* **1986**, *18*, 316.
(39) De Negraro, F. F.; Liano-Ponte, R.; Mondragon, I. *Polymer* **1996**, *37*, 1589.
(40) Heux, L.; Halary, J. L.; Laupretre, F.; Monnarie, L. *Polymer* **1997**, *38*, 1767.
(41) Amdouni, N.; Sautereau, H.; Gerard, J. F.; Pascault, J. P. *Polymer* **1990**, *31*, 1245.
(42) Grillet, A. C.; Galy, J.; Gerard, J. F.; Pascault, J. P. *Polymer* **1991**, *32*, 1885.
(43) Tobolsky, A. V.; Carlson, D. W.; Indicator, N. *J. Polym. Sci.* **1961**, *54*, 175.
(44) Keenan, J. D.; Seferis, J. C. *J. Appl. Polym. Sci.* **1979**, *24*, 2375.
(45) Cukierman, S.; Halary, J. L.; Monnerie, L. *Polym. Eng. Sci.* **1991**, *31*, 1476.
(46) Becker, O.; Varley, R.; Simon, G. *Polymer* **2002**, *43*, 4365.
(47) Colombini, D.; Merle, G.; Martinez-Vega, J. J.; Girare-Reydet, E.; Pascault, J. P.; Gerard, J. F. *Polymer* **1999**, *40*, 935.
(48) Arridge, R. G. C.; Speak, J. H. *Polymer* **1972**, *25*, 1817.
(49) Ochi, M.; Shimbo, M.; Saga, M.; Takashima, N. *J. Polym. Sci.* **1986**, *24*, 2185.
(50) Wang, J. Y.; Ploehn, H. *J. Appl. Polym. Sci.* **1996**, *59*, 345.
(51) Starkweather, H. W. J. *Polymer* **1991**, *32*, 2443.
(52) Starkweather, H. W. J. *Macromolecules* **1990**, *23*, 328.
(53) Qu, W.; Kao, T. M.; Vora, R. H.; Chung, T. S. *Polymer* **2001**, *42*, 6393.
(54) Schroeder, J. A.; Madsen, P. A.; Foister, R. T. *Polymer* **1987**, *28*, 929.
(55) Heux, L.; Halary, J. L.; Laupretre, F.; Monneriev, L. *Polymer* **1997**, *38*, 1767.
(56) Cukierman, S.; Halary, J. L.; Monnerie, L. *J. Non-Crystalline Solids* **1991**, *131*, 898.
(57) Williams, M. L.; Landell, R. F.; Ferry, J. D. *J. Am. Chem. Soc.* **1955**, *77*, 3701.
(58) Ferry, J. D. *Viscoelastic Properties of Polymers*; J. Wiley: New York, 1980.
(59) Musto, P.; Abbate, M.; Ragosta, G.; Scarinzi, G. *Polymer* **2007**, *48*, 3703.
(60) Gerard, J. F.; Galy, J.; Pascault, J. P.; Cukierman, S.; Halary, J. L. *Polym. Eng. Sci.* **1991**, *31*, 615.
(61) Doolittle, A. K.; Doolittle, D. B. *J. Appl. Phys.* **1957**, *28*, 901.
(62) Ragosta, G.; Abbate, M.; Musto, P.; Scarinzi, G.; Mascia, L. *Polymer* **2005**, *46*, 10506.
(63) McCrum, N. G.; Buckley, C. P.; Bucknall, C. B. *Principles of Polymers Engineering*; Oxford Science Publishers: New York, 1997.

MA8005334